

**DISTRIBUTION STATEMENT A**  
Approved for Public Release  
Distribution Unlimited

ISABE 99-7281

**SHOCK REPRESENTATION BY EULER THROUHFLOW MODELS AND  
COMPARISON WITH PITCH-AVERAGED NAVIER-STOKES SOLUTIONS**

A. Sturmayer\* and Ch. Hirsch†

Vrije Universiteit Brussel  
Department of Fluid Mechanics  
1050 Brussels, Belgium

**Abstract**

The shock capturing properties of the axisymmetric Euler throughflow equations in design mode (imposed swirl) and in analysis mode (imposed flow angle) are examined through formulation of the Rankine-Hugoniot relations. A new, hybrid mode is constructed that combines properties of the two classical modes. The consequences of the different shock representation in the several modes are illustrated for five characteristic operating points covering the complete design speed performance curve of a transonic axial compressor rotor. Circumferentially averaged 3D Navier-Stokes solutions serve as a reference. A comprehensive comparison of the throughflow and averaged 3D flow fields is presented. The analysis mode, due to captured shocks, predicts a wrong flow field inside the blade passage, yet is reasonably accurate globally. The design and hybrid modes, due to identical shock capturing properties, give near-identical solutions, which are in excellent agreement with the pitch-averaged 3D reference solutions.

**Notation**

$b$	blockage factor ( $1 - d/s$ )
$C_p$	pressure coefficient
$d$	tangential blade thickness
$E$	total energy per unit mass
$\vec{f}_B$	blade force per unit mass
$\vec{f}_F$	friction force per unit mass
$H$	total enthalpy per unit mass
$I$	unit tensor
$I$	rothalpy per unit mass
$M$	Mach number
$m$	meridional coordinate
$p$	pressure
$\vec{R}$	radius vector $\perp \vec{\Omega}$
$r$	radial coordinate
$S$	surface of volume $V$

\*Research Assistant.

†Professor, Member AIAA.

Copyright © 1999 by Andreas Sturmayer. Published by the American Institute of Aeronautics and Astronautics, Inc. with permission.

$s$	tangential blade spacing
$T$	temperature
$t$	time
$V$	volume
$\vec{W}$	relative velocity vector
$x$	axial coordinate
$\beta$	relative flow angle
$\delta$	deviation angle
$\eta$	efficiency
$\theta$	tangential coordinate
$\Pi$	pressure ratio
$\rho$	density
$\psi$	loss coefficient
$\vec{\Omega}$	vector of angular velocity

**Subscripts**

eff	effective
is	isentropic
ref	reference dynamic quantity
rel	relative
rot	rotary
t	total quantity
LE	leading edge
TE	trailing edge

**1 Introduction**

In recent years, several authors have proposed throughflow models based on the Euler equations, see for instance Spurr (1980), Dawes (1992), Nigmatullin and Ivanov (1994), Boure and Gillant (1995), Yao and Hirsch (1995), Damle et al. (1997), Baralon et al. (1997), and results reported by Vuillez and Petot (1994) and Broichhausen (1994). When solving the Euler equations, the existing, well-developed solution techniques can be applied, the massflow is a result of the computation, choking of blade rows can be predicted, and shocks can be captured. If viscous terms are included, end-wall boundary layers can be computed directly. The important question, however, of what is the most appropriate throughflow representation of supersonic flows and flows with shock waves has not been answered satisfactorily yet. An attempt is therefore made to remedy this situation.

In section 3, the Rankine-Hugoniot relations in de-

sign mode and in analysis mode are derived, starting from the integral formulation of the Euler throughflow equations. Isolation of the prescribed streamwise distribution of either  $W_\theta$  or  $\beta$  as the shock-determining factor leads to the construction of a new mode. Because it combines the off-design analysis capability of the analysis mode with the shock capturing properties of the design mode, this mode is termed hybrid.

In section 4, the practical implications of the different shock capturing properties are discussed. The pitch-averaged representation of a normal shock in a straight 2D blade passage of high stagger angle is compared analytically with the equivalent flow in the two classical throughflow modes, separating the effects of work input (turning) and losses.

Finally, in section 5 the three throughflow modes are put to the test with the NASA Rotor 67 transonic compressor rotor by comparison with pitch-averaged 3D Navier-Stokes solutions for five characteristic design speed operating points ranging from nearly stalled to fully choked.

Conclusions are drawn in section 6 and guidelines formulated for the throughflow calculation of relative supersonic flow with shock capturing Euler models, specifically how to achieve a realistic representation of the pitch-averaged 3D flow field and the correct amount of work input and shock losses.

## 2 The Euler Throughflow Model

The axisymmetric throughflow model is integrated in the 3D Navier-Stokes code Euranus (Hirsch et al.; 1991) and solves the following conservative formulation of the Euler equations:

$$\int_V \frac{\partial}{\partial t} \left| \begin{array}{c} \rho \\ \rho \vec{W} \\ \rho E \end{array} \right| dV + \frac{1}{b} \oint_S \left| \begin{array}{c} b \rho \vec{W} \\ b(\rho \vec{W} \otimes \vec{W} + p \mathbf{I}) \\ b \rho \vec{W} I \end{array} \right| \cdot d\vec{S} = \int_V \left| \begin{array}{c} 0 \\ \rho(\Omega^2 \vec{R} - 2\vec{\Omega} \times \vec{W}) + \rho(\vec{f}_B + \vec{f}_F) + p \frac{\vec{\nabla} b}{b} \\ 0 \end{array} \right| dV \quad (1)$$

The presence of the blades is modelled through a distributed blade force,  $\vec{f}_B$ , to produce the desired turning, through a blockage factor,  $b$ , that accounts for the reduced area due to blade thickness and a distributed friction force,  $\vec{f}_F$ , representing the entropy increase due to losses. The exact blade geometry is not required and the method therefore is suitable for design. In ducts,  $b = 1 = \text{cst}$  and  $\vec{f}_B = \vec{f}_F = 0$ . Eq. (1) is formulated in Cartesian coordinates and solved in the relative system. The finite volume spatial discretization employs either the central scheme or upwind TVD schemes, time integration is explicit through a Runge-Kutta scheme with implicit residual smoothing and multigrid. The mesh consists of a single cell in the tangential direction and does not reflect the

blade geometry; axisymmetry is expressed through a periodic boundary condition.

The blade force  $\vec{f}_B$  is perpendicular to the relative velocity vector. Its magnitude is obtained from an additional time dependent equation, cf. Sturmayer and Hirsch (1999).

The friction force  $\vec{f}_F$  introduces losses in the inviscid flow according to the distributed loss model, Hirsch (1989). It acts in the direction opposite to the relative velocity vector. Its magnitude is proportional to the streamwise derivative of an imposed loss coefficient,  $\partial_m \psi$ , and for the perfect gas its magnitude is given by

$$\rho f_F = \frac{p}{p_{\text{ref}} \partial_m \psi} \quad (2)$$

This formulation ensures that a zero loss coefficient will give exactly zero friction force. In the definition

$$\psi = \frac{p_{\text{t rot LE}} - p_{\text{t rot}}}{p_{\text{ref}}} \quad (3)$$

$p_{\text{ref}}$  is a reference dynamic pressure, taken at the leading edge (for compressors) or trailing edge (for turbines) on each streamwise mesh line, and  $p_{\text{t rot}}$  is the total pressure associated with rothalpy.

## 3 Throughflow Shock Capturing Properties

### 3.1 Preliminary Remarks

For clarity, the discussion is limited to a 2D blade-to-blade section, where the friction force and blockage factor are supposed to vary smoothly across the blade passage. Therefore, they do not enter into the Rankine-Hugoniot relations and will not be considered here.

The 2D Euler equations are reviewed first for reference and the associated throughflow equations then analyzed by imposing axisymmetry and adding the blade force in the right-hand side.

### 3.2 2D Euler Equations

The Euler equations in integral form can be written as

$$\int_V \partial_t \left| \begin{array}{c} \rho \\ \rho \vec{W} \\ \rho E \end{array} \right| dV + \oint_S \left| \begin{array}{c} \rho \vec{W} \\ \rho \vec{W} \otimes \vec{W} + p \mathbf{I} \\ \rho H \vec{W} \end{array} \right| \cdot d\vec{S} = 0 \quad (4)$$

with the relative velocity vector  $\vec{W} = (W_m, W_\theta)^T$ . The Rankine-Hugoniot relations for stationary discontinuity surfaces admitted by system (4) are

$$\begin{aligned} [\rho \vec{W}] \cdot \vec{I}_n &= 0 \\ [\vec{W}] \rho \vec{W} \cdot \vec{I}_n + [p] \vec{I}_n &= 0 \\ [H] &= 0 \end{aligned} \quad (5)$$

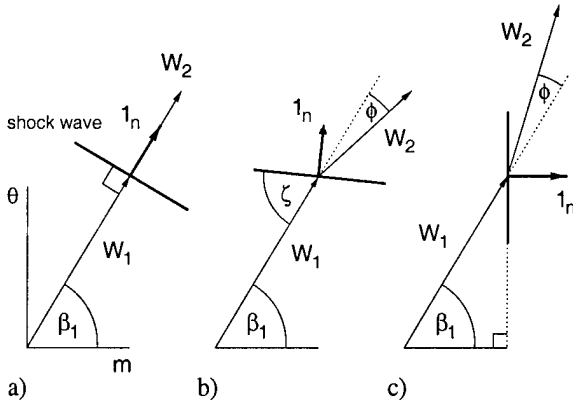


Figure 1: 2D blade-to-blade shock nomenclature: (a) normal shock wave, (b) oblique shock wave, (c) axisymmetric shock wave;  $m$  = meridional direction,  $\theta$  = tangential direction.

with the unit normal vector of the discontinuity surface  $\vec{l}_n = (n_m, n_\theta)^T$ . If  $\vec{l}_n$  is parallel to the flow direction,  $\vec{l}_n = \vec{W}/|\vec{W}|$ , one has a normal shock, Fig. 1a, otherwise an oblique shock, Fig. 1b. A special case of an oblique shock is the axisymmetric shock with  $\vec{l}_n = (1, 0)^T$ , Fig. 1c. This is the only possible shock in the axisymmetric flow in ducts.

### 3.3 Associated Throughflow Equations

With the assumptions of subsection 3.1, of all the throughflow terms of Eq. (1) only the blade force remains. Writing the components of the momentum equation explicitly, this gives

$$\int_V \partial_t \begin{vmatrix} \rho \\ \rho W_m \\ \rho W_\theta \\ \rho E \end{vmatrix} dV + \oint_S \begin{vmatrix} \rho \vec{W} \\ \rho W_m \vec{W} \\ \rho W_\theta \vec{W} \\ \rho H \vec{W} \end{vmatrix} \cdot d\vec{S} + \oint_S \begin{vmatrix} 0 \\ 0 \\ 0 \\ 0 \end{vmatrix} dS_m \\ + \oint_S \begin{vmatrix} 0 \\ 0 \\ p \\ 0 \end{vmatrix} dS_\theta = \int_V \begin{vmatrix} \rho f_{Bm} \\ \rho f_{B\theta} \\ 0 \\ 0 \end{vmatrix} dV \quad (6)$$

The Rankine–Hugoniot relations can either be derived from system (6) directly, or the blade force eliminated first from the differential form of system (6), leaving only one momentum equation. The former way is presented here because it corresponds to the numerical formulation. Both approaches require the definition of the design and analysis problems. The design problem is defined by a smooth streamwise distribution of  $W_\theta$ , thus

$$[W_\theta] = 0 \quad (7)$$

Likewise, the analysis problem is defined by a smooth streamwise distribution of

$$\beta = \text{atan} \frac{W_\theta}{W_m} \quad (8)$$

thus  $[\beta] = 0$  and therefore

$$[W_\theta] = [W_m] \tan \beta \quad (9)$$

In both problems the flow is axisymmetric ( $\partial_\theta = 0$  and  $dS_\theta = 0$ ). The components of the blade force are coupled by the orthogonality condition

$$\vec{f}_B \cdot \vec{W} = 0 \quad (10)$$

The Rankine–Hugoniot relations for stationary discontinuities admitted by system (6) with  $dS_\theta = 0$  are

$$[\rho W_m] = 0 \quad (11)$$

$$\rho W_m [W_m] + [p] = F_{Bm} \quad (12)$$

$$\rho W_m [W_\theta] = F_{B\theta} \quad (13)$$

$$[H] = 0 \quad (14)$$

$F_{Bm}$  and  $F_{B\theta}$  are the components of an impulsive blade force, defined by

$$F_{B\theta} \equiv \lim_{V \rightarrow 0} \int_V \rho f_{B\theta} dV \quad (15)$$

where the control volume  $V$  encloses the discontinuity, and

$$F_{Bm} \equiv \frac{W_{\theta 1} + W_{\theta 2}}{W_{m1} + W_{m2}} F_{B\theta} \quad (16)$$

The subscripts 1 and 2 designate the left and right limit values, for example  $[W_m] = W_{m2} - W_{m1}$ . Definition (16) replaces condition (10), which cannot be applied to  $\vec{F}$  because  $\vec{W}$  is undefined at the discontinuity. Equation (16) implies an arbitrary but realistic choice on the direction of  $\vec{F}$ ; it has no influence on the jump relations of the design and analysis problems.

In the case of the design problem, it follows from Eq. (13) that  $F_{B\theta} = 0$  and further with Eq. (16) that  $F_{Bm} = 0$ . The resulting set of Rankine–Hugoniot relations is the same as that for the 2D Euler equations (5) with  $\vec{l}_n = (1, 0)^T$ ,

$$\begin{aligned} [\rho W_m] &= 0 \\ \rho W_m [W_m] + [p] &= 0 \\ [W_\theta] &= 0 \\ [H] &= 0 \end{aligned} \quad (17)$$

The design problem therefore captures axisymmetric shocks, which requires  $M_m > 1$ .

In the case of the analysis problem, Eq. (13) with  $W_\theta = W_m \tan \beta$  becomes

$$\rho W_m [W_m] \tan \beta = F_{B\theta} \quad (18)$$

$[\tan \beta] = [W_\theta/W_m] = 0$  by definition so that in Eq. (16)  $(W_{\theta 1} + W_{\theta 2})/(W_{m1} + W_{m2}) = W_\theta/W_m$ , yielding

$$F_{Bm} = -\rho W_m [W_m] \tan^2 \beta \quad (19)$$

Inserting  $F_{Bm}$  in Eq. (12) gives the jump relation for axial momentum. The resulting set of Rankine–Hugoniot

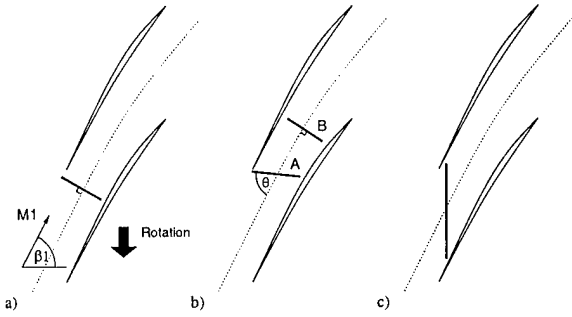


Figure 2: 2D compressor blade passage with supersonic relative inflow ( $M_1 > 1$ ): (a) near stall, (b) choked, (c) axisymmetric shock admitted in design mode if  $M_1 \cos \beta_1 > 1$ .

relations is the same as that for the 2D Euler equations (5) with  $\vec{t}_n = (1, \tan \beta)^T / \sqrt{1 + \tan^2 \beta} = \vec{W} / |\vec{W}|$ ,

$$\begin{aligned} [\rho W_m] &= 0 \\ (1 + a^2) \rho W_m [W_m] + [p] &= 0 \\ [\beta] &= 0 \\ [H] &= 0 \end{aligned} \quad (20)$$

The analysis problem therefore captures normal shocks, which requires  $M_{\text{rel}} > 1$ . It should be stressed that the impulsive force  $\vec{F}$  arises as a result of captured shocks in the analysis problem.

### 3.4 The Hybrid Mode

In the preceding section, a distinction has been made between the design and analysis problems, defined by Eqs. (7) and (9) respectively. Scaling the smooth distributions of respectively  $W_\theta$  or  $\beta$  to fit the LE value and an imposed TE value of that same variable defines the design and analysis modes. The shock capturing properties, however, are defined solely by the choice of the smoothly distributed variable, which may differ from the imposed TE variable. Other modes can therefore be constructed by combining a smoothly distributed variable with a possibly different imposed TE variable. We define the hybrid mode as that mode which combines the shock capturing properties of the design mode with the off-design analysis capability of the analysis mode. The imposed TE variable  $\beta$  is converted to the distributed variable  $W_\theta$  according to

$$W_{\theta \text{ TE}} = |\vec{W}_{\text{TE}}| \sin \beta_{\text{TE}} \quad (21)$$

## 4 The Relevance of Captured Throughflow Shocks

### 4.1 General Considerations

Figure 2 shows selected shocks in the context of a blade-to-blade section of a transonic axial compressor rotor. An

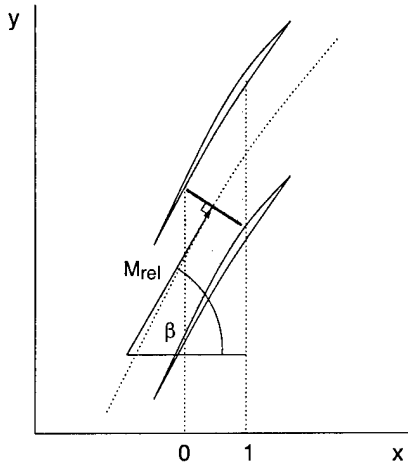


Figure 3: 2D blade-to-blade normal shock at high flow angle.

axisymmetric shock, Fig. 2c, can arise only in axially supersonic flow. In most of today's turbomachinery the flow is axially subsonic, however. The design and hybrid modes then will not capture any shocks. Normal shocks, Fig. 2a and shock B in Fig. 2b, can be captured in analysis mode. Oblique shocks such as shock A in Fig. 2b cannot be captured with either of the two throughflow problems.

Conceptually, the axisymmetric throughflow solution is supposed to represent the pitch-average of the corresponding 3D flow. 3D shocks do not appear as discontinuities in the pitch-average flow unless they are axisymmetric. As Fig. 2 illustrates, their meridional projection may actually cover a substantial fraction of the axial chord. The flow variation across this shock zone in the pitch-average solution and in the throughflow will now be examined analytically for a blade-to-blade normal shock.

### 4.2 Pitch-Averaged Representation of a Blade-to-Blade Normal Shock

Figure 3 shows a normal shock at high flow angle, as it might occur in a transonic rotor. The  $x$ -coordinate has been normalized so that the shock impinges on the pressure surface of the upper blade at  $x = 0$  and on the suction surface of the lower blade at  $x = 1$ . Neglecting blade thickness variation, camber and shock stability questions, the flow upstream and downstream of the normal shock is uniform. The tangential average is then composed of three regions: a uniform region for  $x < 0$ , a smooth transition region for  $0 < x < 1$  and another uniform region downstream for  $x > 1$ .

Figure 4 compares the pitch-averaged 2D blade-to-blade flow with possible throughflow representations for  $\beta = 60^\circ$  and  $M_1 = 1.4$ : (i) a design mode solution with linear swirl ( $W_\theta -$ ) and loss distributions, (ii) a first analysis mode solution with constant flow angle ( $\beta -$ ) and linear loss distributions, (iii) a second analysis mode solution with a captured shock, arbitrarily placed at  $x = 0.3$ .

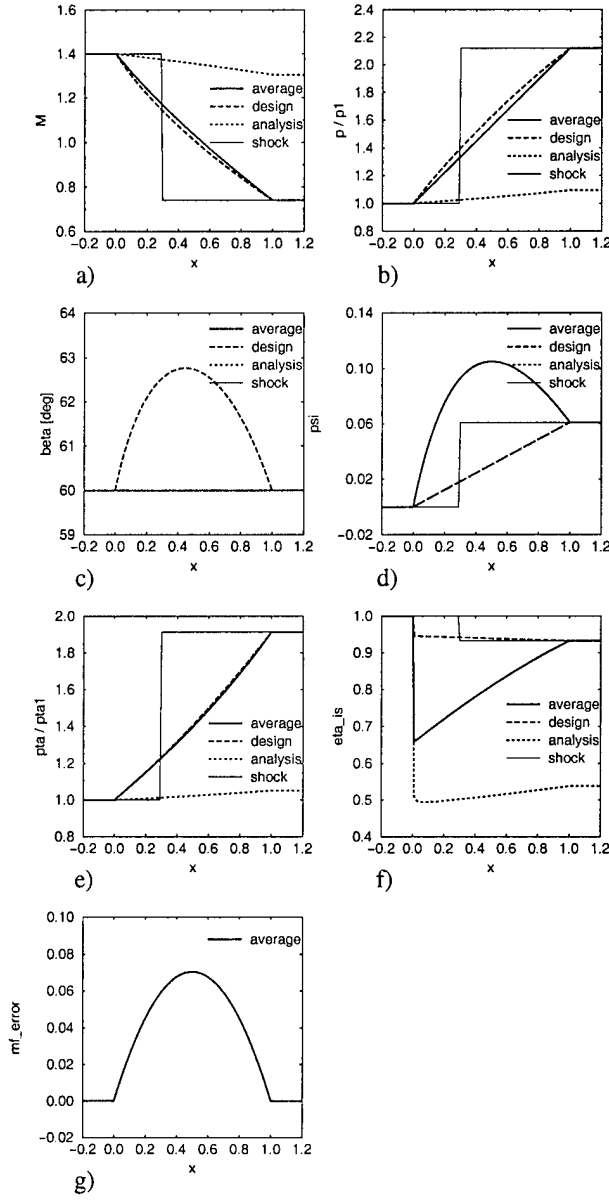


Figure 4: Pitch-averaged representation of a blade-to-blade normal shock and analytical comparison with throughflow for  $\beta = 60^\circ$  and  $M_1 = 1.4$ : (a) Mach number, (b) pressure ratio, (c) relative flow angle, (d) loss coefficient, (e) absolute total pressure ratio, (f) isentropic efficiency, (g) massflow error.

The pitch-averaged solution is defined by the area averaged primitive variables. (For this flow configuration, area and mass averaging are the same.) The effect of a captured shock in analysis mode, shown as a light line in Figs. 4a-f, is identical to that of the blade-to-blade normal shock. However, the ensuing discontinuity compares poorly with the smooth variation observed in the averaged solution, considering, for instance, Mach number

and static pressure ratio, Figs. 4a and b. These same figures also show the agreement between the design mode solution (bold dashed line) and the actual average (bold solid line). In the other analysis mode solution, the flow remains supersonic because the equations associated with  $\beta = \text{cst}$  and imposed losses describe one-dimensional adiabatic flow at constant area, which evolves along the Fanno line. In the average and in the design mode solution, deceleration to subsonic is enabled by two different mechanisms. In the latter, the flow angle does not remain constant inside the shock zone, Fig. 4c, the maximum deflection amounting to  $2.8^\circ$ , while in the former there is a considerable overshoot in the loss coefficient to nearly twice the final value, Fig. 4d.

Figures 4e and f show the total pressure ratio and efficiency that would result if the shock occurred in a rotor with axial inflow. In analysis mode with a captured shock, both are exact upstream and downstream of the shock zone, but discontinuous, while with imposed losses and constant flow angle both are unrealistically low. The design mode, by contrast, agrees perfectly with the averaged solution in terms of pressure ratio, Fig. 4e, and gives an even better approximation of efficiency, Fig. 4f, because the loss overshoot in the averaged solution causes a corresponding undershoot in efficiency.

The primitive-variable-averaged 2D solution does not satisfy the 1D conservation laws, Fig. 4g. A conservative average can, however, be defined (not shown here for clarity), and this would be practically indistinguishable from the design mode solution, including the flow deflection throughout the shock zone.

### 4.3 Captured Shocks in Analysis Mode

Practically, there appears to be little latitude in controlling captured shocks. Their structure is determined primarily by the streamwise flow angle distribution, somewhat by the geometrical blade blockage, with minor influence from the imposed losses and their streamwise distribution. Flow angle and thickness distributions must conform to the actual ones found in the pitch-averaged solution because they fix the choking massflow. Therefore, no parameter is left to control the shock pattern, which has to be accepted as is and an attempt is made to exclude the associated losses from the imposed ones.

## 5 Transonic Axial Compressor Results

### 5.1 Test Case Description

The effect of the different shock capturing properties in design mode, in analysis mode and in hybrid mode will now be examined at the example of NASA Rotor 67 (Strazisar et al.; 1989; Fottner; 1990). This is a typical transonic compressor rotor, with the design parameters listed in Table 1.

This test case has been chosen in part because of the availability of numerical data in the form of eleven 3D

Table 1: NASA Rotor 67 design parameters.

Pressure ratio	1.63
Efficiency	91 %
Inlet tip Mach number	1.38
Tip stagger angle	64 deg
Number of blades	22
Aspect ratio	2.25
Mean hub/tip radius ratio	0.427

Navier–Stokes solutions covering the complete performance curve. Those computations had been performed with the same flow solver on a mesh of circa 550,000 cells, Fig. 6a, including tip clearance and with a two-equation turbulence model. Five characteristic operating points were selected: near stall (NS), mid-range (MR), peak efficiency (PE), near choke (NC) and choked at a low pressure ratio (CH).

Fig. 5 schematically shows the blade modelling parameters. The flow path and leading and trailing edge geometry are represented exactly in the throughflow mesh of  $32 \times 72 = 2304$  cells, Fig. 6b. The mesh is uniform, with  $32 \times 32$  cells in the blade passage. This mesh size has been determined in a mesh sensitivity study to guarantee a sufficiently low level of numerical dissipation.

The spanwise profile of maximum blade thickness,  $d_{\max}$ , was obtained from the blade geometry. The location of  $d_{\max}$  is at 60 % axial chord at the tip and 50 % at the hub, with a linear transition. The streamwise blade thickness distribution is quadratic (power function with exponent 2).

## 5.2 Analysis of the Pitch-Averaged 3D Flow

The pitch-averaged solution is defined by the mass averaged primitive variables. Figures 6c–f show the spanwise profiles of incidence angle, deviation angle, exit swirl and loss coefficient extracted from the pitch-averaged

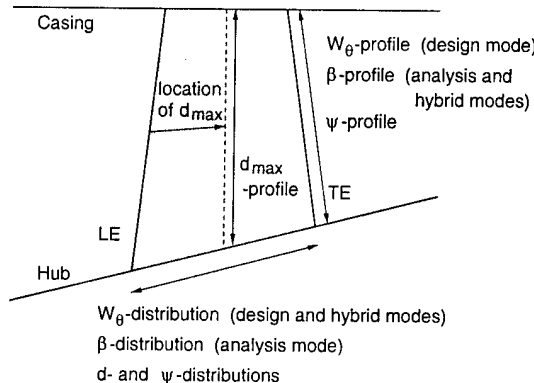


Figure 5: Throughflow blade modelling parameters.

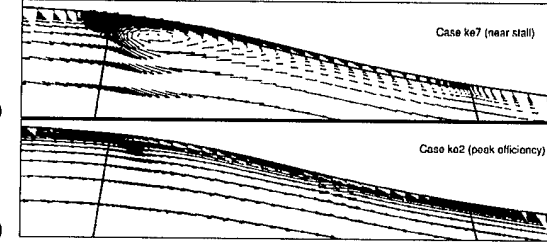


Figure 7: Detail of the pitch-averaged calculated 3D velocity field at the blade tip: (a) near stall, (b) at peak efficiency.

3D Navier–Stokes solutions for the five operating points. Because normal shocks are expected to be captured in analysis mode, the associated losses (the captured shock losses) were approximatively removed from the loss profiles imposed in analysis calculations by subtracting the losses of a normal shock at the inlet Mach number, the latter being assumed to vary linearly from 1 at 40 % span (measured from the hub) to 1.4 at the casing. Near stall, a vortex forms at the LE tip, Fig. 7a (caution: the figure does not show the flow in the tip gap proper but the circumferentially averaged flow in the tip region; the blade contours are drawn to aid orientation.) The ensuing recirculation zone extends along the casing beyond the TE, causing considerable end-wall blockage. Corrections therefore had to be made to the swirl and loss profiles for this operating point near the casing (the bold straight line segments in Figs. 6e and f), smoothing out strong local variations to give profiles close to the mixed out ones one chord downstream. The LE tip vortex is negligible for the four other operating points, Fig. 7b; in particular, there is no backflow at the TE. The extracted profiles could therefore be used directly.

Figure 8 compares the streamwise distributions for  $\beta$ ,  $W_\theta$  and  $\psi_{\text{rot}}$  at three spanwise positions (12 %, 52 % and 88 % span from the hub) with power functions for selected exponents (5, 2, 1.2, 1, -1.2, -2, -5). Four of the five selected operating points are shown: NS, PE, NC and CH. In the throughflow model, the same power function distribution applies to all spanwise locations. Figure 8 indicates that this is a good approximation in most cases. S-shaped distributions, such as the choked swirl distribution, Fig. 8h, and overshoots, such as in the choked flow angle distribution, Fig. 8d, cannot be represented by the current simple power function model. Based on these figures and past experience, a  $\beta$ -exponent of 2 was chosen for all operating points (analysis mode) and  $W_\theta$ -exponents of 2, 1.75, 1.5, 1 and again 1 for the near stall, mid-range, peak efficiency, near choke and choked at low pressure ratio operating points, respectively (design and hybrid modes). The loss distribution, within the reasonable bounds observed in Figs. 8i–k, is not a sensitive parameter and was therefore chosen linear for all cases ( $\psi$ -exponent 1).

An exception had to be made for the choked operating point at low pressure ratio (CH). Contrary to the

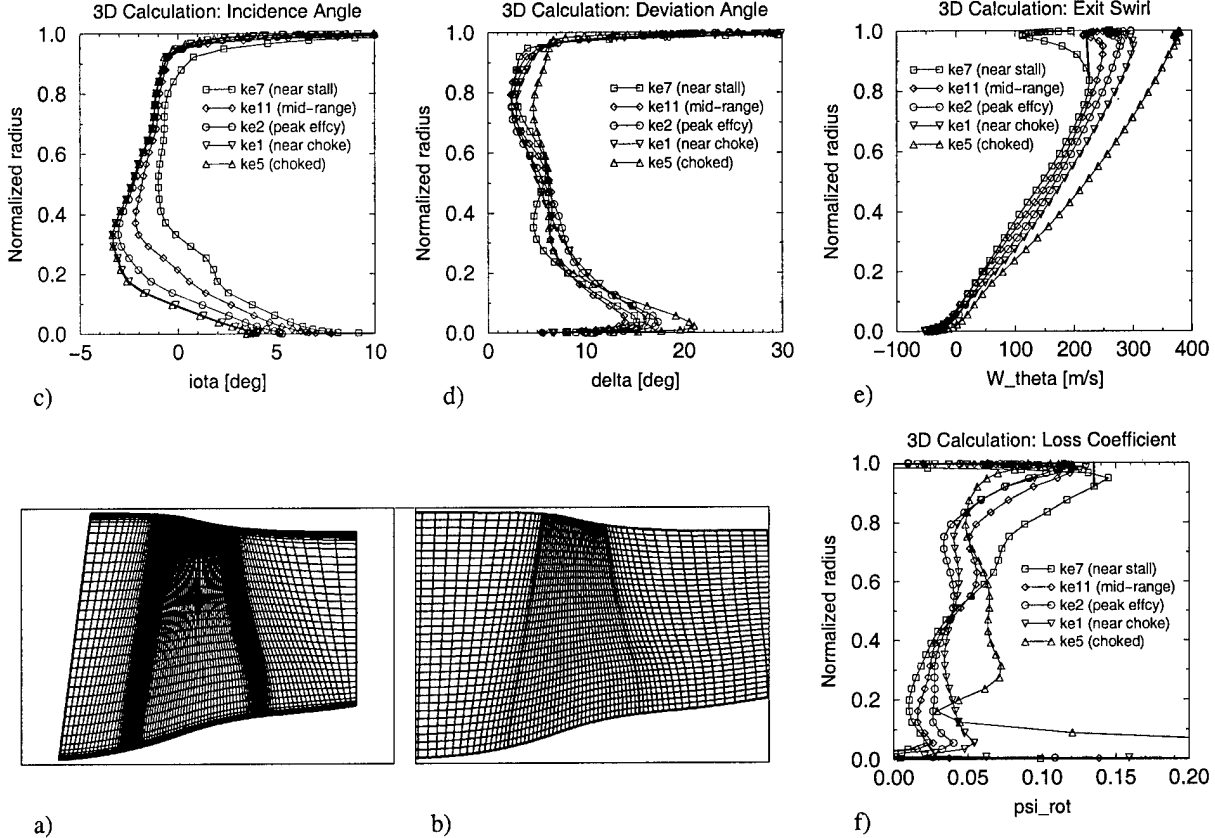


Figure 6: Computational grids: (a) Meridional projection of the 3D Navier–Stokes mesh, (b) the Euler throughflow mesh. Spanwise profiles extracted from the pitch-averaged 3D solutions: (c) incidence angle with respect to the blade suction side, (d) deviation angle, (e) relative tangential velocity at the blade trailing edge, (f) loss coefficient.

design mode, the analysis mode has a built-in choking mechanism. A linear loss distribution leads to losses in the forward part of the blade passage which, near the hub and at mid-span, are too high compared with the actual values, Fig. 8l. With the ensuing diminished total pressure, the blade passage throat can pass only a reduced massflow; compared with the NC operating point, the choking massflow obtained with a linear loss distribution is underpredicted by 2 %. A consistent value is obtained with the power function exponent  $-2.5$  suggested by Fig. 8l. The analysis of the pitch-averaged 3D flow field thus provides both qualitative and quantitative information on the streamwise distributions of flow angle or swirl, and losses. Although they have little impact on the downstream flow, they are important for the flow field inside the blade passage and the choking massflow in analysis mode.

In accordance with the analysis performed in section 4, features of the pitch-averaged streamwise distributions of Fig. 8 can be associated with the various oblique and normal shocks in the blade-to-blade plane. As an example, Fig. 9 shows pressure and Mach contours at the same three spanwise positions. At 88 % span, Fig. 9a, expansion of the supersonic flow along the slightly cambered

suction surface together with the deflection through the oblique bow shock cause significant overturning, Fig. 8d. This is undone by the oblique passage shock which emanates from the suction side of the trailing edge and is reflected off the pressure surface. This reflected shock and another weak oblique shock originating from the trailing edge extend into the downstream region. Work input, Fig. 8h, is smooth and continuous. Losses rise steeply where shock strength is high (at and immediately downstream of the leading edge) and where the percentage of axial chord covered by the circumferential projection of oblique shocks is small (the passage shock is of roughly the same strength as the bow shock — both have an upstream Mach number of 1.45 and similar obliquity — but its projected length, between  $x \approx 0.7$  and 1, is smaller than that of the bow shock, between  $x \approx 0$  and 0.8). Similar reasoning can be applied to the mid-span and hub sections, Figs. 9b and c. Here, it is the normal or near-normal passage shock that accounts for most of the losses, Fig. 8l, with only minimal losses upstream.

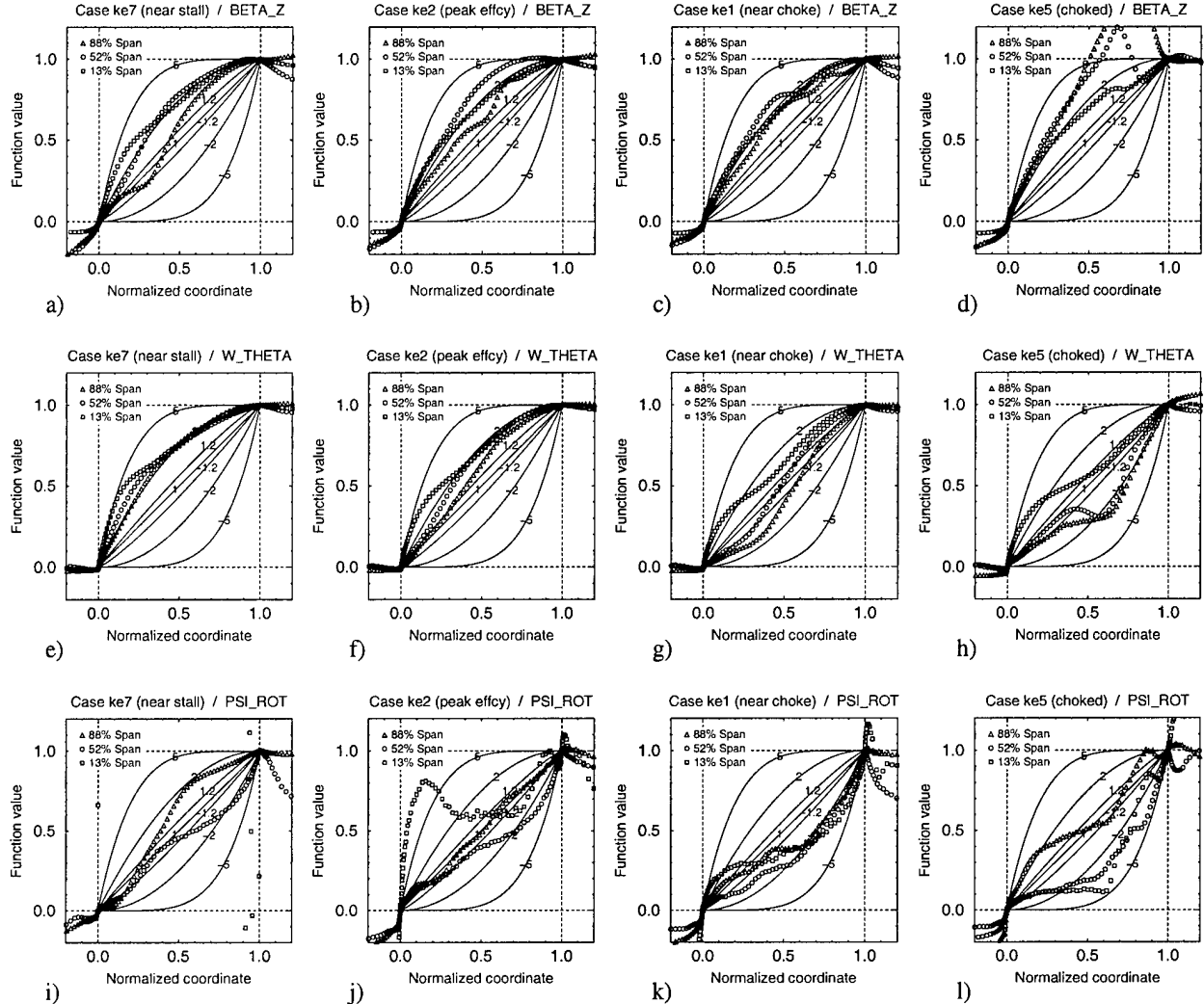


Figure 8: Streamwise distributions extracted from the pitch-averaged 3D solutions at three spanwise sections compared to power functions: top row = relative flow angle ( $\beta$ ), middle row = relative tangential velocity ( $W_\theta$ ), bottom row = loss coefficient ( $\psi_{\text{rot}}$ ); outer left column = near stall (NS), inner left column = peak efficiency (PE), inner right column = near choke (NS), outer right column = choked (CH); in detail: (a)  $\beta$  NS, (b)  $\beta$  PE, (c)  $\beta$  NC, (d)  $\beta$  CH, (e)  $W_\theta$  NS, (f)  $W_\theta$  PE, (g)  $W_\theta$  NC, (h)  $W_\theta$  CH, (i)  $\psi_{\text{rot}}$  NS, (j)  $\psi_{\text{rot}}$  PE, (k)  $\psi_{\text{rot}}$  NC, (l)  $\psi_{\text{rot}}$  CH; triangles = near the casing (88 % span), circles = at mid-span (52 %), squares = near the hub (13 % span), solid lines = power functions with exponents 5, 2, 1.2, 1, -1.2, -2, -5.

### 5.3 Throughflow Calculation Strategy

Each of the five selected operating points was calculated in each of the three throughflow modes as follows:

In design mode, the imposed exit swirl fixes the work input (up to the effect of radial streamline displacement with varying back pressure). Because the flow remains axially subsonic, the design mode does not have a built-in choking mechanism. Variation of the exit pressure therefore results in horizontal displacement of the operating points in the performance diagrams: the massflow adapts, at nearly constant pressure ratio and efficiency.

Both analysis mode and hybrid mode do have a built-

in choking mechanism: the fixed flow angle limits the effective area available to the relative flow, expressed by the blockage factor  $b_{\text{eff}}$ , according to

$$b_{\text{eff}} = b \cos \beta \quad (22)$$

Even though in 3D the situation is complicated by AVDR variation for individual blade-to-blade sections, the same reasoning applies for the blade passage as a whole. In analysis mode, the CH and NC operating points were run to the correct pressure ratio. The three non-choked operating points (PE, MR and NS) were then run to the correct fraction of the choking massflow. The same proce-

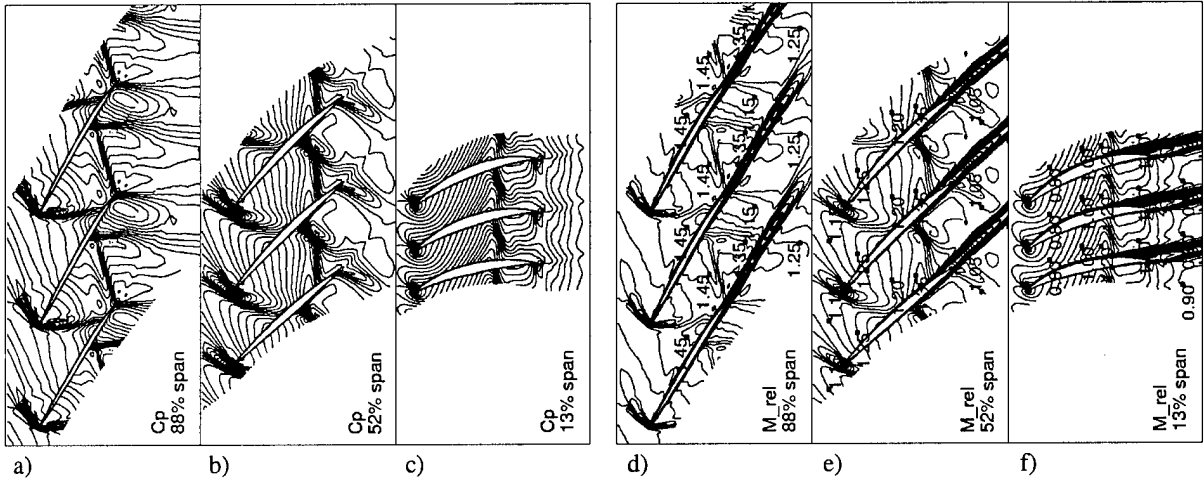


Figure 9: For the choked operating point (CH), pressure contours (a) near the casing, (b) at mid-span, (c) near the hub, and Mach contours (d) near the casing, (e) at mid-span, (f) near the hub.

dure was followed in hybrid mode, except for NC, which was run to the correct fraction of choking massflow because its choking massflow (i.e., that obtained with the NC profiles instead of the CH profiles, but with the same streamwise distributions) turned out to be higher than that of CH.

Figure 10 compares the resulting performance curves with those of the reference 3D Navier-Stokes calculations.

Also shown are the measured performance curves. A discussion of possible reasons for the discrepancy between the 3D calculation and the experimental data is beyond the scope of this paper. The reference for the throughflow calculations are the calculated 3D results, because this is from where the input profiles have been taken.

Each curve has been normalized with respect to its own choking massflow. All lie within 2 % of the experimental value. While the design and hybrid modes agree remarkably well with the reference 3D calculation, the analysis mode overestimates both pressure ratio and efficiency of the non-choked operating points. This is explained by the presence of multiple shocks, to be discussed below, and the modified loss profiles. The shock pattern is insensitive to the imposed losses. Even though one might be tempted to conclude that the captured shock losses have been overestimated when removing them from the extracted ones, it should not be forgotten that the presence of multiple shocks has of course a profound impact on AVDR. The correct exit angle does therefore not guarantee the correct exit swirl and thus work input.

#### 5.4 Comparison with Pitch-Averaged 3D Flow Fields

Figures 11–14 compare the flow fields obtained in analysis mode and in design mode with the pitch-averaged cal-

culated 3D flow field through  $M_{\text{rel}}$ ,  $C_p$ ,  $\beta$  and  $W_\theta$ . The hybrid mode is shown in Fig. 15. Figures 11–14 show in the left-hand column the analysis mode, in the central column the pitch-averaged 3D solution and in the right-hand column the design mode. In all five figures, the sequence of rows, from top to bottom, is composed of the NS, PE, NC and CH operating points.

A first overview suggests that, except for the flow angle, Fig. 13, design mode and analysis mode differ dramatically inside the blade passage and that the design mode better approximates the pitch-averaged 3D flow field.

In accordance with theory, the design mode does not capture shocks, because the axial Mach number remains subsonic. An exception is the CH operating point, for which a weak shock appears to be captured at the blade root at 2/3 chord, Figs. 11l and 12l. Incidentally, this is also the location of the passage shock in 3D. Between the hub and mid-span, this passage shock is nearly axisymmetric and consequently appears as a near-discontinuity in the pitch-average, Figs. 11k and 12k.

The analysis mode, independently of the operating point, captures a normal shock at the blade leading edge, Figs. 11, 12 and 14. For all operating points except the NS one, this is followed by a second normal shock at or near the trailing edge. Going along the performance curve from stall to choke (the sequence of figures 11a, d, g, j), the reacceleration to supersonic flow and the strength and inboard extension of the second shock intensify. This process is associated with a downstream displacement of the second shock, which gradually moves off the blade, thereby allowing the required supersonic exit flow in the outboard region at choked operation, Fig. 11j.

Despite the differences inside the blade passage, the downstream flow fields in design and analysis mode are nearly the same, and in very good agreement with the reference 3D solution. This observation holds unreservedly

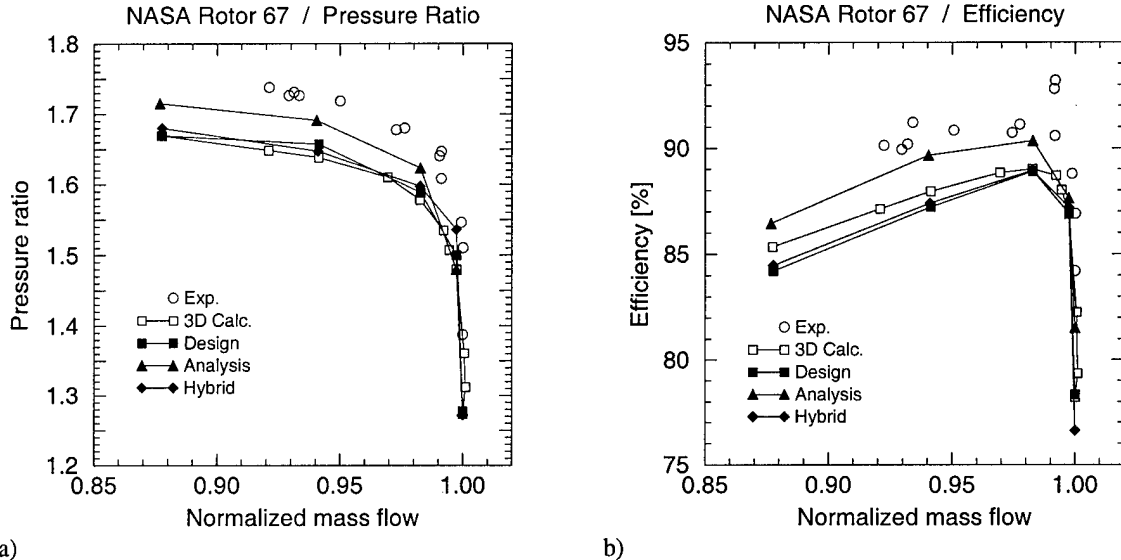


Figure 10: NASA Rotor 67 performance curves: (a) absolute total pressure ratio, (b) isentropic efficiency; open circles = experiment, open squares = 3D calculation, filled squares = design mode, filled triangles = analysis mode, filled diamonds = hybrid mode.

for Mach number and  $C_p$ , for the NS and PE operating points. Near stall, the averaged 3D flow has a low velocity/recirculation zone at the blade tip that gradually mixes out, Fig. 11b, see also Fig. 7. It is caused by phenomena in the blade-to-blade plane and interaction with the tip leakage flow and does therefore not arise in the throughflow calculations, Figs. 11a and c. Near choke, distinctions begin to appear in the downstream field, in the form of additional expansion/acceleration in the lower 60–70 % span, which is not observed in the averaged 3D solution and more pronounced in analysis mode than in design mode, Figs. 11g–l and 12g–l.

Another interesting feature of the averaged 3D flow on which both throughflow solutions necessarily miss out is the effect of wake blockage and mixing, cf. Fig. 9d–f. This is most visible at the blade root, immediately downstream of the trailing edge, from the hub to about 30 % span, Figs. 11 and 12. Here, the throughflow isoline patterns of both  $M_{\text{rel}}$  and  $C_p$  are ‘centered’ about the trailing edge, while in the averaged 3D solution the pattern is shifted some way downstream. This also has consequences on the flow angle, Fig. 13. The representation of wake blockage in the throughflow might therefore be desirable because it would allow a more realistic throughflow representation. On the other hand, it would add an additional modelling parameter to be tuned or correlated.

The fact that the smooth compression in the forward part of the blade passage, Figs. 11b,e and 12b,e, is so well represented in the design solution, Figs. 11c,f and 12c,f, is due to the realistic choice of streamwise  $W_\theta$ –distribution that could be made for these cases, Figs. 8e and f. For distributions which cannot be well represented by the simple power functions, e.g., those near choke (NC), Figs.

8g and 11h, 12h, agreement is less good, Figs. 11i, 12i. S-shaped  $W_\theta$ –distributions prevail in this range, with steeper gradients and therefore isoline clustering in the middle of the blade, while the best-compromise linear distribution of the throughflow produces uniform deceleration. If this kind of information is available, it might be worth while to allow more detailed throughflow modelling via independent control of the hub, mid-span and tip regions, and via two-piece power functions.

However, the error made by simplified streamwise  $W_\theta$ –distributions in design mode is much smaller than that caused by the captured shocks in analysis mode, and its consequences on the downstream flow are presumably negligible. The latter is not true of the analysis mode, where the flow angle field is visibly distorted downstream of the second, trailing edge shock, Figs. 13d,g,j. The best agreement, for all operating points, is given by the hybrid mode, Figs. 15b,e,h,k. Conformity with 3D is even particularly good for choked operation at low pressure ratio, Figs. 13k and 15k, where the unturning at about 3/4 chord is well reproduced, also, in slightly milder form, in design mode, Fig. 13l. This effect is captured without any tuning of the  $W_\theta$ –distribution, which is linear for the NC and CH operating points. In the analysis solution it is necessarily absent, Fig. 13j. Inside the blade passage, design mode and hybrid mode yield correct swirl fields, Figs. 14 and 15c,f,i,l, while the analysis mode deviates strongly where shocks are captured, from about 50 % span to the casing.

To avoid arbitrary modification of the extracted profiles, it was left to the Euler throughflow mesh to filter out end-wall boundary layer effects. The high flow angles near the stationary casing extend far enough inward

to be partially visible on the throughflow mesh, however. As a consequence, both the analysis and the hybrid solutions have a zone of low and even negative turning at the casing, Fig. 13, left column, and Fig. 15, central column. Owing to diffusion on the Euler mesh, the low-turning zone spreads radially inwards downstream of the blade row.

## 6 Conclusions

The shock capturing properties of the Euler throughflow equations have been determined through analysis of the Rankine–Hugoniot relations. The design mode captures axisymmetric shocks, the analysis mode quasi-normal shocks.

The shock capturing properties were found to depend only on the streamwise distributed variable, not on the variable for which a trailing edge profile is imposed. This enabled the construction of a novel mode, termed the hybrid mode, which combines the imposed trailing edge flow angle of the analysis mode with the shock capturing properties of the design mode.

For an isolated 2D blade-to-blade section, analysis mode and design mode have been analytically compared with the pitch-averaged representation of a normal shock at high flow angle, showing the deviation of the analysis mode from the averaged solution.

3D Navier–Stokes solutions of a transonic axial compressor rotor for different operating points have been analyzed in detail with regard to the profiles and distributions required as input to the throughflow model. Throughflow calculations in the three modes were then performed with the extracted swirl (design mode) or flow angle (analysis and hybrid modes) and loss profiles. It is concluded that

(1) the analysis mode captures a normal shock at the leading edge and, depending on the operating point, a second normal shock near the trailing edge.

(2) As a consequence of this, the blade passage flow field in the upper half-span is not correctly represented in analysis mode.

(3) The smooth, continuous deceleration in the pitch-averaged 3D solution is correctly represented by the design mode and by the hybrid mode.

(4) Despite the erroneous solution inside the blade passage, the downstream flow field in analysis mode is largely correct.

(5) Design mode and hybrid mode converge two to four times faster than the analysis mode, for transonic flows with captured shocks.

## References

Baralon, S., Eriksson, L.-E. and Hall, U. (1997). Viscous Throughflow Modelling of Transonic Compressors Using a Time-Marching Finite Volume Solver, 13th International Symposium on Airbreathing Engines (ISABE), Chattanooga, USA.

Boure, G. and Gillant, P. (1995). Aerodynamic Modelling of a Transonic Radial Equilibrium of a Multistage Compressor, *Turbomachinery—Fluid Dynamic and Thermodynamic Aspects*, VDI Berichte 1185, pp. 143–155.

Broichhausen, K. (1994). Aero Design of Turbomachinery Components — CFD in Complex Systems, in A. S. Üçer (ed.), *Turbomachinery Design Using CFD*, AGARD-LS-195, chapter 9.

Damle, S. V., Dang, T. Q. and Reddy, D. R. (1997). Throughflow Method for Turbomachines Applicable for All Flow Regimes, *Transactions of the ASME, Journal of Turbomachinery* 119(2): 256–262.

Dawes, W. N. (1992). Toward Improved Throughflow Capability: The Use of Three-Dimensional Viscous Flow Solvers in a Multistage Environment, *Transactions of the ASME, Journal of Turbomachinery* 114: 8–17.

Fottner, L. (ed.) (1990). *Test Cases for Computation of Internal Flows in Aero Engine Components*, AGARD-AR-275.

Hirsch, C. (1989). *Numerical Computation of Internal and External Flows*, Vol. 1: Fundamentals of Numerical Discretization, John Wiley & Sons.

Hirsch, C., Lacor, C., Rizzi, A., Eliasson, P., Lindblad, I. and Häuser, J. (1991). A Multiblock/Multigrid Code for the Efficient Solution of Complex 3D Navier–Stokes Flows, Presented at the First European Symposium on Aerothermodynamics for Space Vehicles.

Nigmatullin, R. Z. and Ivanov, M. J. (1994). The mathematical models of flow passage for gas turbine engines and their components, *Mathematical Models of Gas Turbine Engines and their Components*, AGARD-LS-198, chapter 4.

Spurr, A. (1980). The Prediction of 3D Transonic Flow in Turbomachinery Using a Combined Throughflow and Blade-to-Blade Time Marching Method, *International Journal of Heat and Fluid Flow* 2(4): 189–199.

Strazisar, A. J., Wood, J. R., Hathaway, M. D. and Suder, K. L. (1989). Laser Anemometer Measurements in a Transonic Axial-Flow Fan Rotor, NASA Technical Paper 2879.

Sturmayr, A. and Hirsch, C. (1999). Through-Flow Model for Design and Analysis Integrated in a 3D Navier–Stokes Solver, *Turbomachinery: Fluid Dynamics and Thermodynamics, Volume A*, Proceedings of the Third European Conference on Turbomachinery (IMechE), London, pp. 501–515. To be published in the Proceedings of the Institution of Mechanical Engineers, Part A: Journal of Power and Energy.

Vuillez, C. and Petot, B. (1994). New Methods, New Methodology — Advanced CFD in the SNECMA Turbomachinery Design Process, in A. S. Üçer (ed.), *Turbomachinery Design Using CFD*, AGARD-LS-195, chapter 7.

Yao, Z. and Hirsch, C. (1995). Throughflow Model Using 3D Euler or Navier–Stokes Solvers, *Turbomachinery—Fluid Dynamic and Thermodynamic Aspects*, VDI Berichte 1185.

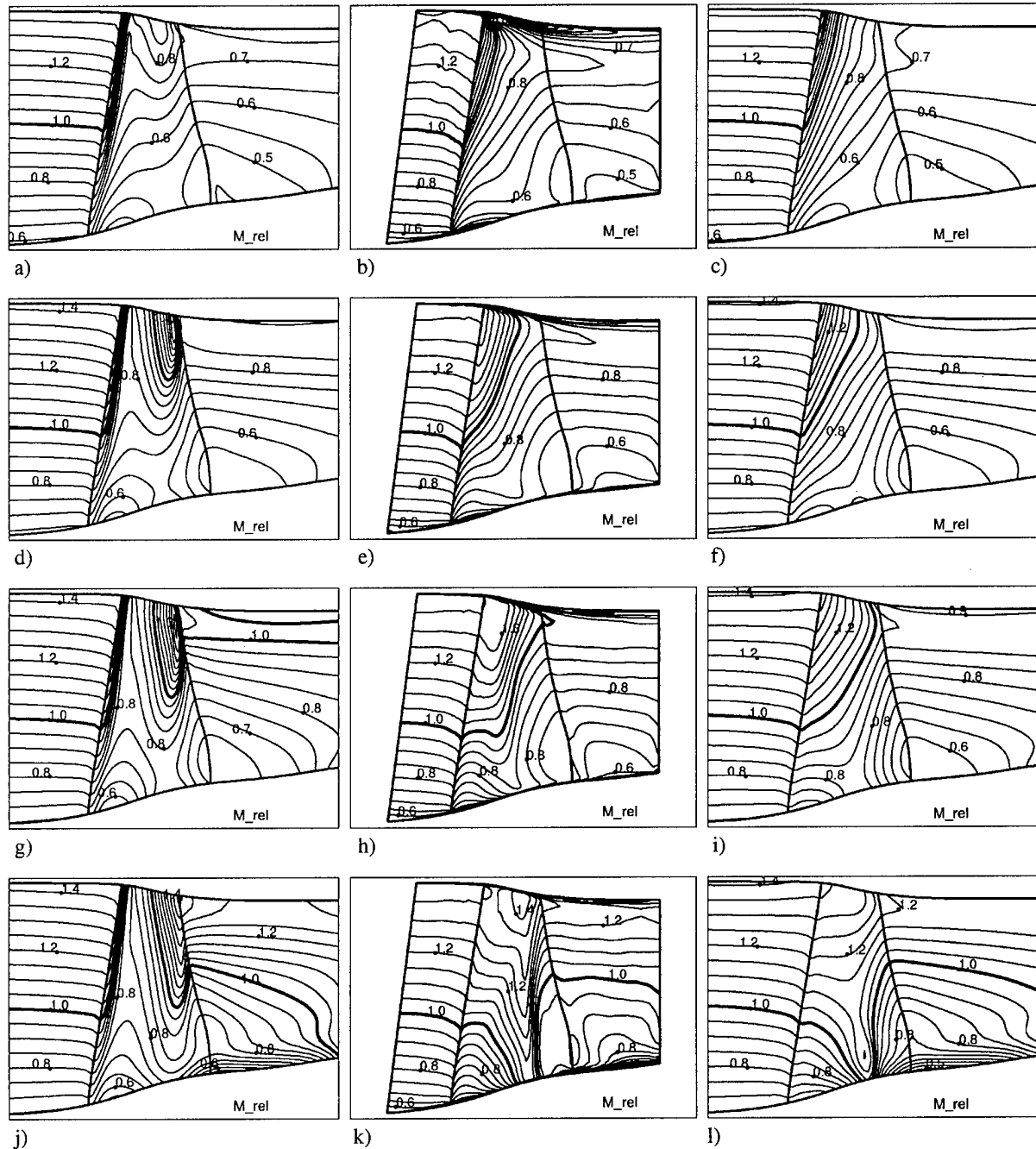


Figure 11: NASA Rotor 67, isolines of relative Mach number ( $M_{rel}$ , increment 0.05): left column = analysis mode, central column = pitch-averaged 3D solution, right column = design mode; first row from top = near stall (NS), second row = peak efficiency (PE), third row = near choke (NC), fourth row = choked (CH); in detail: (a) NS analysis, (b) NS 3D, (c) NS design, (d) PE analysis, (e) PE 3D, (f) PE design, (g) NC analysis, (h) NC 3D, (i) NC design, (j) CH analysis, (k) CH 3D, (l) CH design.

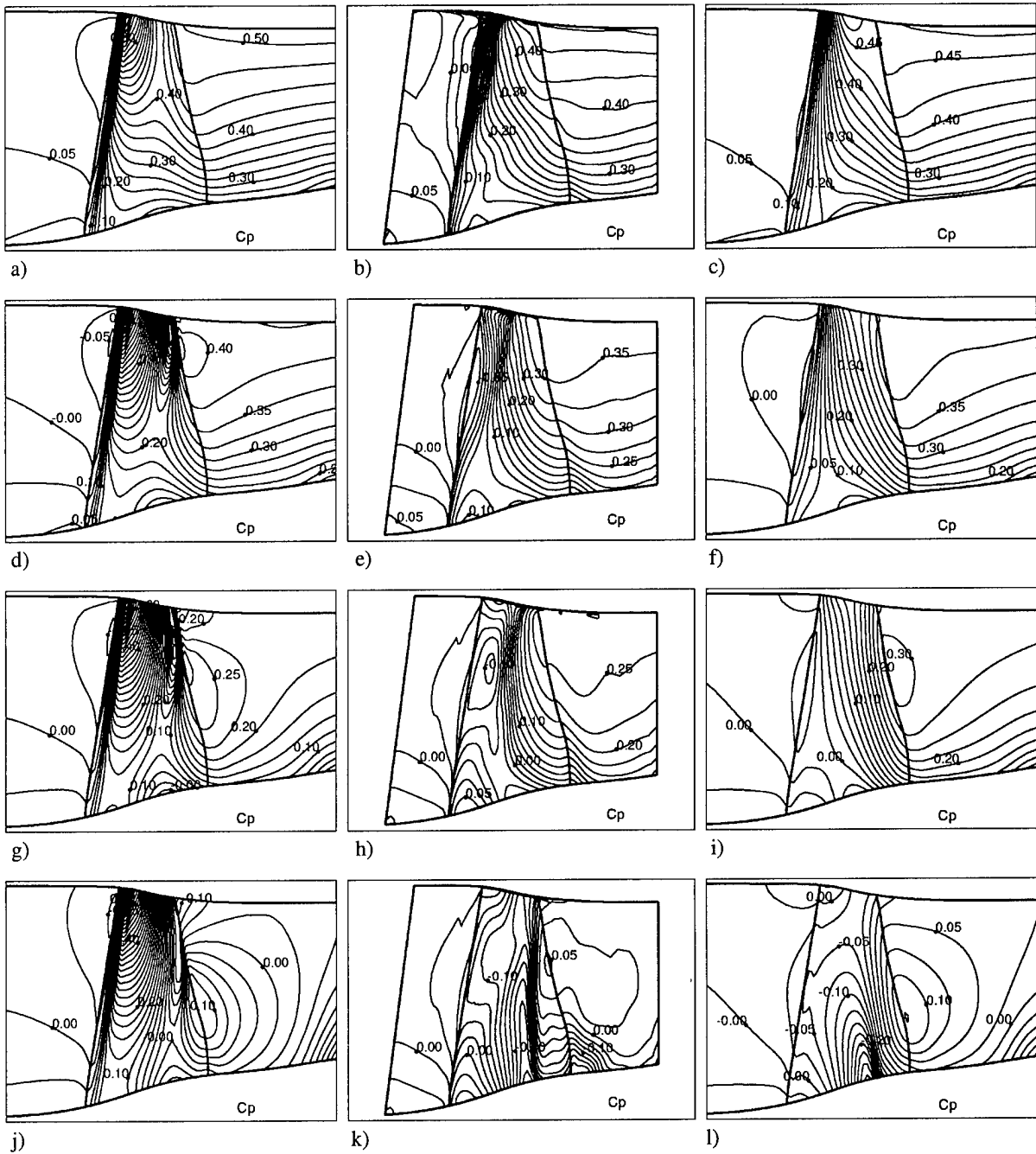


Figure 12: NASA Rotor 67, isolines of static pressure coefficient ( $C_p$ , increment 0.025): left column = analysis mode, central column = pitch-averaged 3D solution, right column = design mode; first row from top = near stall (NS), second row = peak efficiency (PE), third row = near choke (NC), fourth row = choked (CH); in detail: (a) NS analysis, (b) NS 3D, (c) NS design, (d) PE analysis, (e) PE 3D, (f) PE design, (g) NC analysis, (h) NC 3D, (i) NC design, (j) CH analysis, (k) CH 3D, (l) CH design.

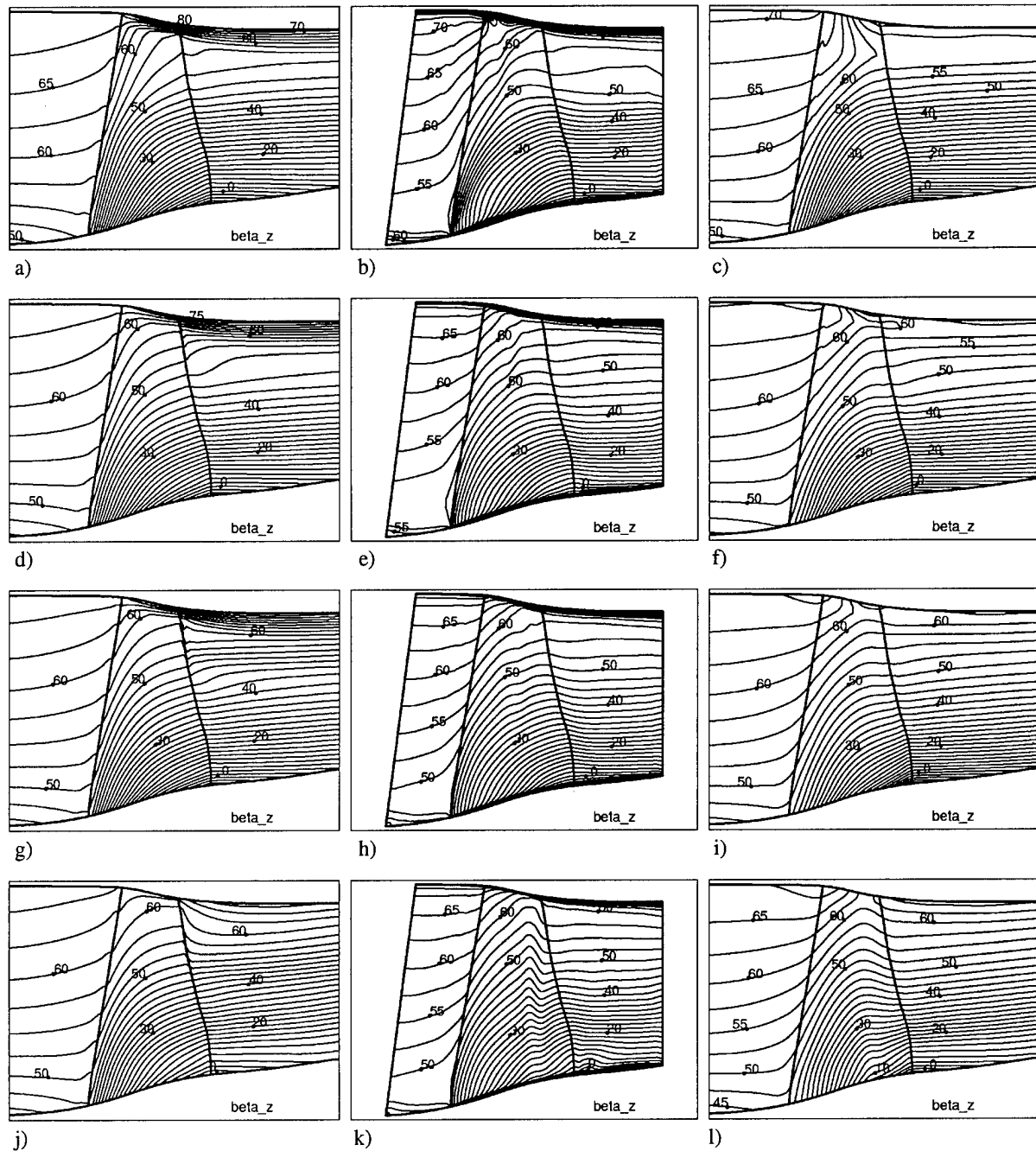


Figure 13: NASA Rotor 67, isolines of relative flow angle ( $\beta$  in deg, increment 2.5 deg): left column = analysis mode, central column = pitch-averaged 3D solution, right column = design mode; first row from top = near stall (NS), second row = peak efficiency (PE), third row = near choke (NC), fourth row = choked (CH); in detail: (a) NS analysis, (b) NS 3D, (c) NS design, (d) PE analysis, (e) PE 3D, (f) PE design, (g) NC analysis, (h) NC 3D, (i) NC design, (j) CH analysis, (k) CH 3D, (l) CH design.

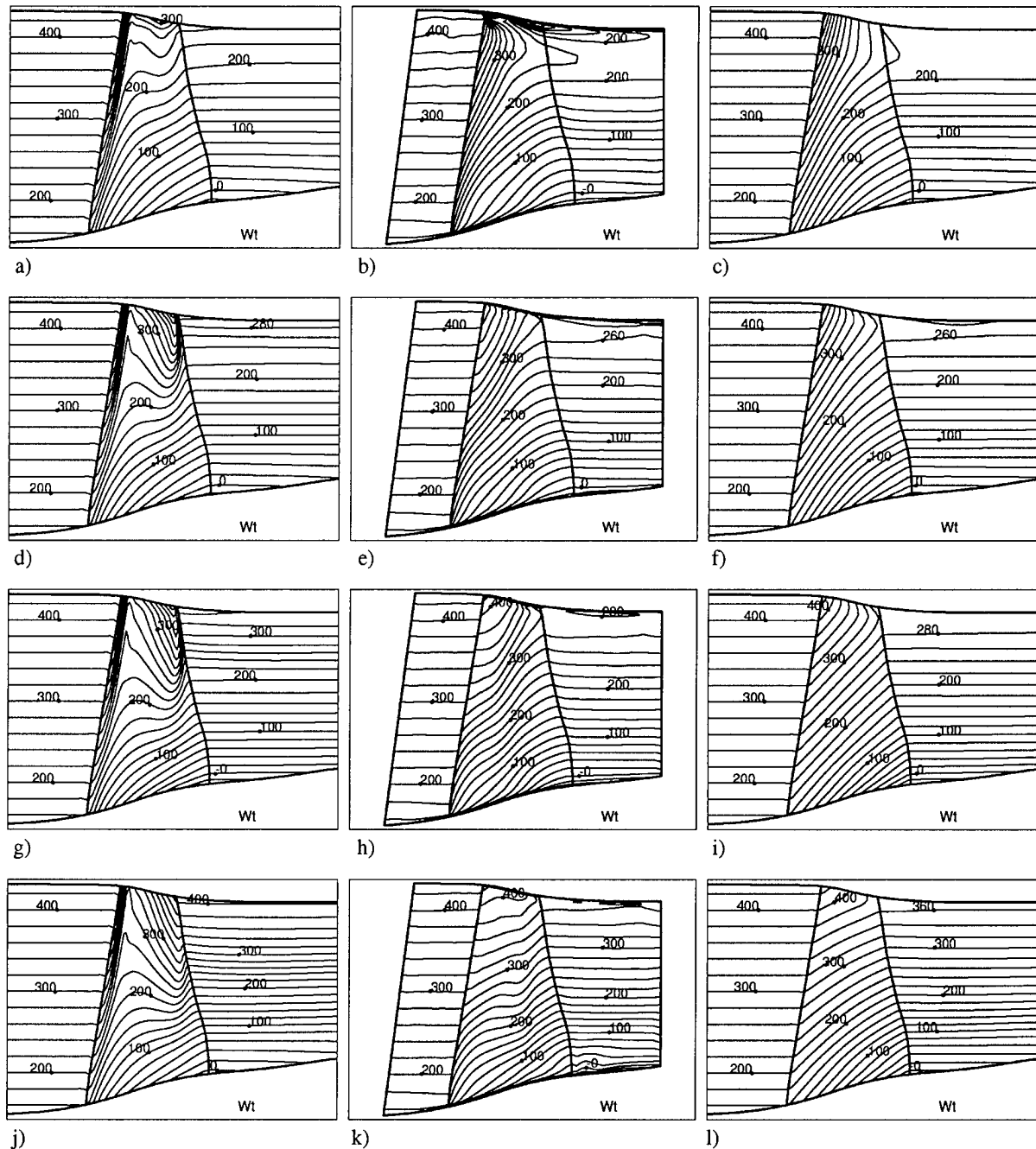


Figure 14: NASA Rotor 67, isolines of relative tangential velocity ( $W_t$  in m/s, increment 20 m/s): left column = analysis mode, central column = pitch-averaged 3D solution, right column = design mode; first row from top = near stall (NS), second row = peak efficiency (PE), third row = near choke (NC), fourth row = choked (CH); in detail: (a) NS analysis, (b) NS 3D, (c) NS design, (d) PE analysis, (e) PE 3D, (f) PE design, (g) NC analysis, (h) NC 3D, (i) NC design, (j) CH analysis, (k) CH 3D, (l) CH design.

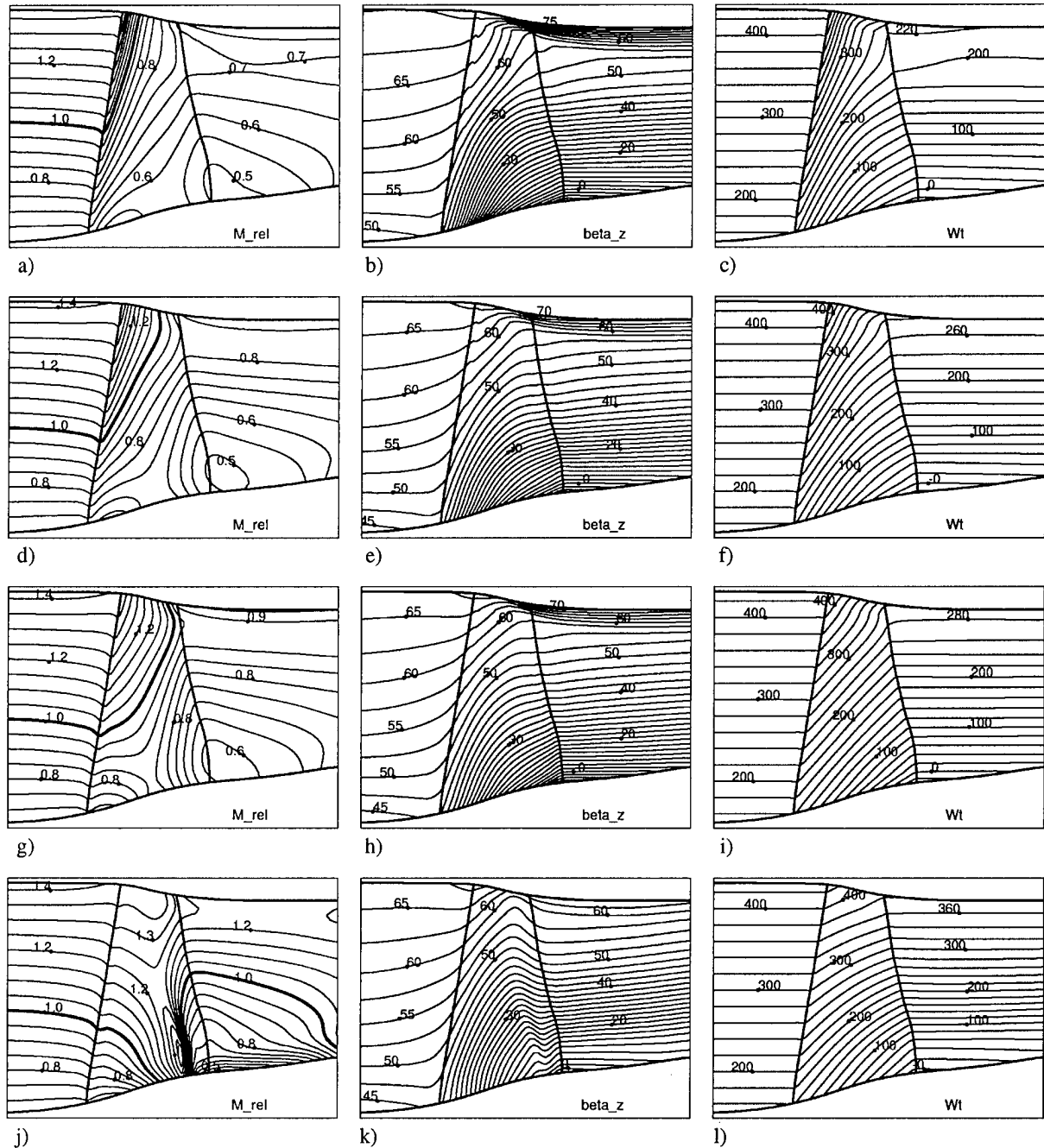


Figure 15: NASA Rotor 67, hybrid mode: left column = relative Mach number ( $M_{rel}$ , increment 0.05), central column = relative flow angle ( $\beta$  in deg, increment 2.5 deg), right column = relative tangential velocity ( $W_t$  in m/s, increment 20 m/s); first row from top = near stall (NS), second row = peak efficiency (PE), third row = near choke (NC), fourth row = choked (CH); in detail: (a) NS  $M_{rel}$ , (b) NS  $\beta$ , (c) NS  $W_t$ , (d) PE  $M_{rel}$ , (e) PE  $\beta$ , (f) PE  $W_t$ , (g) NC  $M_{rel}$ , (h) NC  $\beta$ , (i) NC  $W_t$ , (j) CH  $M_{rel}$ , (k) CH  $\beta$ , (l) CH  $W_t$ .